arXiv:2009.03214v2 [cond-mat.str-el] 7 Oct 2020

Realising square and diamond lattice $S = 1/2$ Heisenberg antiferromagnet models in the α and β phases of the coordination framework, $KTi(C_2O_4)_2{\cdot}xH_2O$

Aly H. Abdeldaim,[1,2,3] Teng Li,[4] Lewis Farrar,[1] Alexander A. Tsirlin,[5,6] Wenjiao Yao,[4,7] Alexandra S. Gibbs,[3] Pascal Manuel,[3] Philip Lightfoot,[4] Gøran J. Nilsen,[3] and Lucy Clark[1,2,*]

[1] *Department of Chemistry and Materials Innovation Factory, University of Liverpool, 51 Oxford Street, Liverpool, L7 3NY, UK*
[2] *School of Chemistry, University of Birmingham, Edgbaston, Birmingham B15 2TT, UK*
[3] *ISIS Neutron and Muon Source, Science and Technology Facilities Council, Didcot OX11 0QX, UK*
[4] *School of Chemistry, University of St. Andrews, St. Andrews KY16 9ST, UK*
[5] *Theoretical Physics and Applied Mathematics Department, Ural Federal University, 620002 Yekaterinburg, Russia*
[6] *Experimental Physics VI, Center for Electronic Correlations and Magnetism, Institute of Physics, University of Augsburg, 86135 Augsburg, Germany*
[7] *Functional Thin Films Research Center, Shenzhen Institutes of Advanced Technology, Chinese Academy of Sciences, Shenzhen 518055, China*

We report the crystal structures and magnetic properties of two psuedo-polymorphs of the $S = 1/2$ Ti^{3+} coordination framework, $KTi(C_2O_4)_2{\cdot}xH_2O$. Single-crystal X-ray and powder neutron diffraction measurements on α-$KTi(C_2O_4)_2{\cdot}xH_2O$ confirm its structure in the tetragonal $I4/mcm$ space group with a square planar arrangement of Ti^{3+} ions. Magnetometry and specific heat measurements reveal weak antiferromagnetic interactions, with $J_1 \approx 7$ K and $J_2/J_1 = 0.11$ indicating a slight frustration of nearest- and next-nearest-neighbor interactions. Below 1.8 K, α-$KTi(C_2O_4)_2{\cdot}xH_2O$ undergoes a transition to G-type antiferromagnetic order with magnetic moments aligned along the c axis of the tetragonal structure. The estimated ordered moment of Ti^{3+} in α-$KTi(C_2O_4)_2{\cdot}xH_2O$ is suppressed from its spin-only value to 0.62(3) μ_B, thus verifying the two-dimensional nature of the magnetic interactions within the system. β-$KTi(C_2O_4)_2{\cdot}2H_2O$, on the other hand, realises a three-dimensional diamond-like magnetic network of Ti^{3+} moments within a hexagonal $P6_222$ structure. An antiferromagnetic exchange coupling of $J \approx 54$ K—an order of magnitude larger than in α-$KTi(C_2O_4)_2{\cdot}xH_2O$—is extracted from magnetometry and specific heat data. β-$KTi(C_2O_4)_2{\cdot}2H_2O$ undergoes Néel ordering at $T_N = 28$ K, with the magnetic moments aligned within the ab plane and a slightly reduced ordered moment of 0.79 μ_B per Ti^{3+}. Through density-functional theory calculations, we address the origin of the large difference in the exchange parameters between the α and β psuedo-polymorphs. Given their observed magnetic behaviors, we propose α-$KTi(C_2O_4)_2{\cdot}xH_2O$ and β-$KTi(C_2O_4)_2{\cdot}2H_2O$ as close to ideal model $S = 1/2$ Heisenberg square and diamond lattice antiferromagnets, respectively.

I. INTRODUCTION

The discovery of new magnetic materials allows for the realization of theoretical ground state predictions as well as the identification of novel emergent phenomena. Both rely on a fine balance between several material "ingredients" that determine the magnetic properties, including exchange frustration[1], low-dimensionality[2], and spin-orbit coupling[3]. Systems based on the $S = 1/2$ Heisenberg frustrated square lattice (FSL) model, for example, are extensively studied as they provide a rich magnetic phase diagram depending on the degree of frustration between exchange interactions along the sides, J_1, and across the diagonal, J_2, of the square net. For the antiferromagnetic phase diagram[4], theoretical predictions for the development of Néel and columnar antiferromagnetic orders within the respective dominant J_1 or J_2 regimes have been experimentally established in several materials[5–13]. Intriguingly, at the border of these two regimes, materials in which the degree of frustration is maximized—*i.e.* $0.4 < J_2/J_1 < 0.6$—are predicted to map a region of the phase diagram within which a quantum spin liquid (QSL) ground state is realized [14–16]. Indeed, in a recent theoretical and experimental investigation of the solid-solution, $Sr_2Cu(Te_{1-x}W_x)O_6$ where $x = 0$ and $x = 1$ represent Néel and columnar ordered systems, respectively, QSL signatures have been observed for the $x = 0.5$ compound[17]. Interestingly, the behavior exhibited by complex materials derived from the FSL, such as $BaCdVO(PO_4)_2$[6], where signatures of a spin-nematic ground state have been observed in an applied field[18, 19], has further enriched the phase diagram of FSL materials, leading to new theoretical predictions[20]. By extending the $J_1 - J_2$ model to incorporate the effects of interplanar coupling, J_3, magnetic ground states inaccessible to the pure FSL model can also be realized[21].

While often sought within manifestations of low-dimensional models, the three-dimensional diamond lattice offers an alternative route towards unconventional magnetic ground states. Recent investigations of A-site spinels have revived interest in the Heisenberg frustrated diamond lattice (FDL) model following the experimental

* Email address: l.m.clark@bham.ac.uk

observation of spin-spiral structures[22] and spin-liquid regimes[23, 24]. As such structures indicate exchange competition, this behavior can be ascribed to the presence of a frustrated further-neighbor coupling, J_2, beyond the nearest-neighbor interaction, J_1. Beyond the theoretically predicted critical point at $J_2/J_1 > 0.125$, a set of degenerate spin-spiral states were found to describe a novel spin-liquid regime[25]. Signatures of this dynamic behavior have been observed in material realizations of the J_1-J_2 FDL model, such as in $MnSc_2S_4$[24] and $CoAl_2O_4$[26], where theory combined with experimental diffuse neutron scattering studies conclude the presence of a continuous spin-spiral surface in momentum space[23, 24]. Perturbations further enrich the magnetism of such FDL systems, and spin-orbit coupling [27–29], further-neighbor couplings, and structural distortions[22] can play a significant role in determining the magnetic ground state.

In this vein, alternative chemical realizations of highly sought magnetic models can be achieved through the synthesis of coordination framework materials. When compared to their inorganic counterparts, the versatility of possible organic linkers in coordination frameworks offers a wider command over the dimensionality and magnetic properties of the magnetic sublattice[30, 31]. Indeed, a range of architectures, ranging from the star lattice[32], to square[33] and diamond networks[34] have been prepared in coordination frameworks.

Motivated by the richness of intriguing behavior exhibited within the FDL and FSL models, we here explore a Ti^{3+}-based coordination framework realization of a diamond lattice, β-$KTi(C_2O_4)_2.2H_2O$ (β), in addition to identifying its previously predicted [35] square planar network pseudo-polymorph, α-$KTi(C_2O_4)_2{\cdot}xH_2O$ (α). We report the crystal structures, thermodynamic properties, and magnetic structures of both pseudo-polymorphs using a combination of single-crystal X-ray diffraction, powder neutron diffraction, magnetic susceptibility, specific heat measurements, and *ab initio* calculations. Beginning with Section. II, we present our synthetic route for micro- and polycrystalline samples and summarize our experimental methods. In Sec. III, we identify the crystal structure of α and provide evidence for the quasi-two-dimensional behavior of this non-stoichiometric hydrate. This is followed by a discussion of our structural and magnetic investigation of β in Sec. IV. A discussion of the electronic structure calculations, single-ion properties, and exchange pathways of both compounds ensues in Sec. V. Finally, we conclude in Sec. VI and provide an outlook for future experiments.

II. EXPERIMENTAL METHODS

Polycrystalline samples of α and β were synthesized hydrothermally according to modified versions of previously published methods [36, 37]. In a typical synthesis of either sample, an aqueous solution of K_2CO_3 (Sigma Aldrich 99.99%) and $H_2C_2O_4{\cdot}2H_2O$ (Sigma Aldrich > 99.5%) was prepared in a round bottom flask and heated to 343 K (α) or 363 K (β) under constant stirring. After 1 hour of sparging with N_2 gas, $TiCl_3$ (Sigma Aldrich $\geq$ 12% $TiCl_3$ basis) was introduced to the solution, and either an orange or a maroon colored precipitate immediately formed for α and β, respectively. The reaction proceeded for 30 minutes, after which the round bottom flask was quenched in an ice bath. The resulting product was collected by filtration and washed with acetone. The molar ratios of K_2CO_3, $H_2C_2O_4 \cdot 2H_2O$, $TiCl_3$, and H_2O used were $1:3:5:277$ and $2:6:1:1000$ for α and β, respectively. It should be noted that the β phase appears to be more thermodynamically stable as if not immediately collected from solution, samples of α slowly recrystallize into β. Deuterated samples of α-$KTi(C_2O_4)_2{\cdot}xD_2O$ were synthesized using D_2O. Deuteration of β was not achieved. While products are air-stable for short periods ($\approx$ 1 day), handling in an inert environment is necessary to avoid H-D exchange.

Single-crystal X-ray diffraction (SC-XRD) measure-

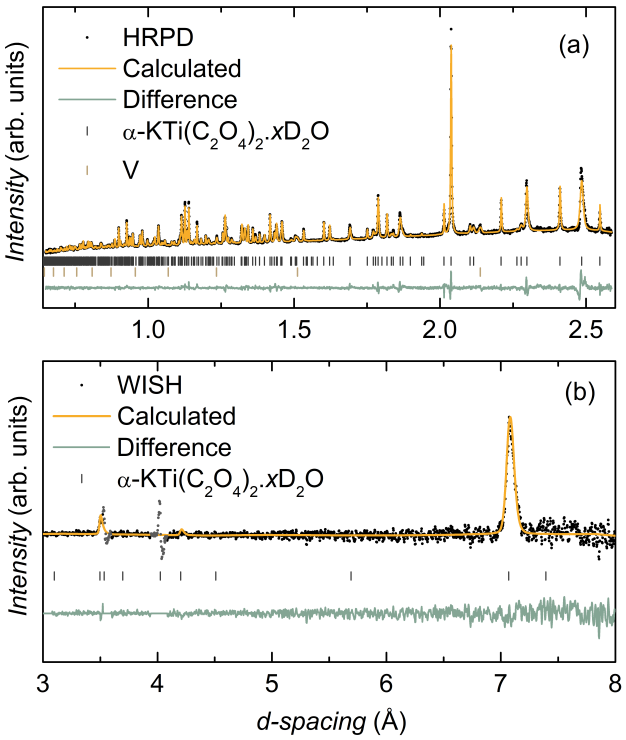

FIG. 1. (a) Rietveld refinement of the $I4/mcm$ model ($\chi^2 = 4.80$, $R_p = 2.83\%$) describing the structure of deuterated α-$KTi(C_2O_4)_2{\cdot}1.48(4)D_2O$ using data collected on the HRPD instrument at 1.8 K. (b) Rietveld plot ($\chi^2 = 1.81$ and $R_{mag} = 3.16\%$) of the $I4/m'cm$ magnetic structure to magnetic only scattering obtained by subtracting data collected on the WISH instrument at 15 K from 1.2 K data. In both plots, data points are shown in black, fitted curves in orange, difference curves in blue, Bragg reflection positions in grey and brown, and excluded data points in grey.

ments were performed at 150 K using a Bruker D8 VENTURE diffractometer equipped with a PHOTON-II detector and a Mo $K\alpha$ source with $\lambda = 0.71073$ Å using ω scans. The reduction and integration of the collected data were performed using the `APEX III` software package. Structure solutions were obtained using direct methods by utilizing `SHELXT-2013` [38] followed by refinements using `SHELXL-2013`[39] on the `OLEX2` software with multi-scan absorption correction. Non-hydrogen atoms were modeled with anisotropic displacement parameters.

Powder neutron diffraction (PND) data[40] were collected on the time-of-flight High-Resolution Powder Diffractometer (HRPD)[41] at the ISIS Neutron and Muon Source. Vanadium-windowed flat plate sample containers were used, and measurements were carried out on 2 g samples of each compound at 1.8 K and 300 K. All three fixed angle detector banks (centered around 168°, 90°, and 30°) were used for the nuclear structural refinement. To probe the magnetic structures of α and β, PND data[42] were collected for the same 2 g samples using the long wavelength WISH diffractometer [43] at the ISIS Neutron and Muon Source. Cylindrical vanadium containers were used, and measurements were carried out at 1.2 K, 2 K, 3 K, 4 K, 6 K, and 15 K for α and at 1.2 K and 35 K for β. Rietveld refinements of the nuclear and magnetic structures were conducted on the `GSAS`[44, 45] and `FULLPROF`[46] software packages, respectively. Instrumental impurity phases (*i.e.* steel and vanadium) were modeled using the Le Bail method.

Temperature-dependent DC magnetic susceptibility data were measured on 13.21 mg (α) and 38.09 mg (β) samples using both field cooled and zero-field cooled protocols in a 0.1 T applied field between 1.8 K and 300 K using a Quantum Design MPMS 3 SQUID magnetometer. Specific heat data were recorded in a temperature range of 1.8 K to 300 K in zero-field on a Quantum Design PPMS DynaCool using 9.11 mg and 6.71 mg pressed powder samples of α and β, respectively.

Quantum Monte Carlo (QMC) simulations were performed using the directed loop (`loop`)[47, 48] algorithm of the `ALPS`[49, 50] simulation package. The temperature dependence of the magnetic susceptibility and specific heat were calculated for a 60×60 square lattice model (2×60^2 spins) with 10^5 thermalization and sweep steps. The high-temperature-series expansion (HTE) of the $S = 1/2$ FSL and FDL models were calculated using the [4,6] Padé approximants derived from the `HTE10`[51] code.

Fully relativistic density-functional theory (DFT) band-structure calculations were performed in the `FPLO` code[52] using Perdew-Wang approximation for the exchange-correlation potential[53]. States near the Fermi level were used to construct Wannier functions, analyze their composition, and calculate hopping parameters t_i that determine the antiferromagnetic superexchange $J_i = 4t_i^2/U$, where U is the on-site Coulomb repulsion parameter. A well-converged **k**-mesh with 242 irreducible **k**-points for the α and 168 **k**-points for the β were used. The experimentally determined crystallographic model was employed for β. In contrast, calculations for α required the construction of ordered models, owing to the partially disordered arrangement of K^+ and H_2O between the $[Ti(C_2O_4)_2]^-$ layers (see Fig. S1(a) of the Supplemental Material [54]). Three models were considered: (i) K^+ ions on the four-fold rotation axis and two water molecules per formula unit ($I4/m$) [Fig. S1(b)], (ii) K^+ ions on the four-fold rotation axis, no water molecules ($I4/mcm$) [Fig. S1(c)], and (iii) K^+ ions occupying half of their experimental positions, with no water molecules ($Ima2$) [Fig. S1(d)]. All three models produced very similar results for the bands around the Fermi level and led to essentially indistinguishable Ti^{3+} Wannier functions, suggesting that the positions of K^+ ions and water molecules have no significant influence on the magnetism of the system.

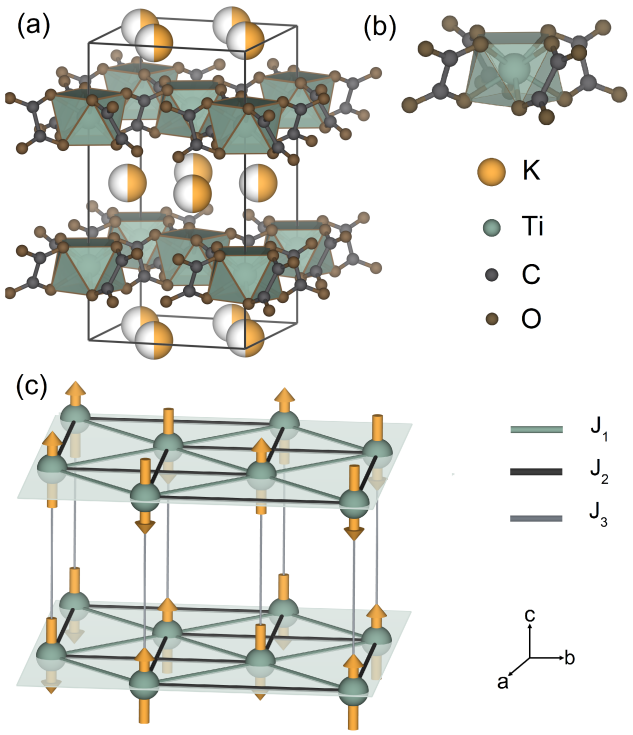

FIG. 2. (a) The crystal structure of α-$KTi(C_2O_4)_2{\cdot}xH_2O$ as viewed along the [111] direction where the (b) oxalate-bridged square antiprismatic Ti^{3+} ions form square planar sheets within the ab plane separated by a disordered layer of orange K^+ ions and water molecules which are omitted for clarity. (c) G-type antiferromagnetic ordering of the magnetic moments obtained from the analysis of PND data at 1.2 K, where the orange Ti^{3+} magnetic moments lie along the crystallographic c axis with nearest-neighbor (J_1), next-nearest-neighbour (J_2), and interplanar (J_3) exchange interactions highlighted in black, blue, and gray, respectively. Both structures were generated using the `VESTA`[55] visualization software.

III. RESULTS FOR α-$KTi(C_2O_4)_2{\cdot}xH_2O$

A. Crystal Structure

Analysis of SC-XRD data collected at 150 K reveals that diffraction patterns of α can be indexed by the tetragonal space group $I4/mcm$. The refined parameters within this model are presented in Table. I. Through a multibank Rietveld analysis of PND data collected for a deuterated sample of α on HRPD, the $I4/mcm$ model was verified at both 1.8 K and 300 K. A single deuterium site was located on a Fourier difference map, at a location similar to that obtained from SC-XRD, and refined according to an O-D bond distance restraint (0.97(3) Å). The refinement was initially carried out with the occupancy of the water site fixed to 0.5, as obtained from SC-XRD, to represent a dihydrate, yielding $\chi^2 = 7.23$ and $R_p = 3.45\%$. A significant improvement to the fit [Fig. 1(a)] is obtained, however, when the occupancy of the water site is varied resulting in $\chi^2 = 4.80$ and $R_p = 2.83\%$. The refinement converges to a non-stoichiometric hydrate occupancy of 0.37(1) (*i.e.* α-$KTi(C_2O_4)_2{\cdot}1.48(4)D_2O$), with the rest of the refinement parameters presented in Table II.

The resulting crystal structure is consistent with that predicted by Drew *et al.*[35], and is illustrated in Fig. 2(a). It is composed of two-dimensional layers of oxalate-bridged square antiprismatic Ti^{3+} ions separated by a disordered layer of K^+ ions and water molecules along the c axis with an interplanar Ti-Ti distance of 7.36(1) Å. Each square antiprism is coordinated by four oxalate molecules in the ab plane [Fig. 2(b)] which results in a square planar arrangement with nearest-neighbor Ti-Ti superexchange, J_1, [Fig. 2(c)] mediated *via* the Ti-O-C-O-Ti pathway at a distance of 5.69(1) Å. The next-nearest-neighbor coupling, J_2 [Fig. 2(c)], runs along the $\langle 010 \rangle$ directions at a Ti-Ti distance of 8.05(1) Å.

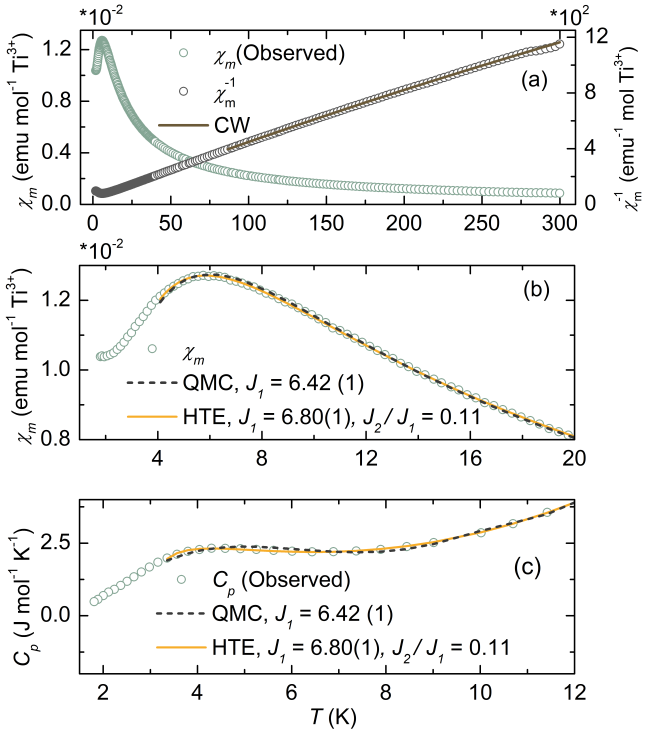

FIG. 3. (a) Temperature-dependent zero-field cooled magnetic susceptibility, χ_m (blue), of α measured in an applied field of 0.1 T and its inverse, χ_m^{-1} (grey). A modified Curie-Weiss fit (brown) to χ_m^{-1} yields $C = 0.233(1)$ emu K mol^{-1}, $\theta_{CW} = -7.86(1)$ K, and $\chi_0 = 1.19(2) \times 10^{-4}$ emu mol^{-1}. Quantum Monte Carlo (grey) and tenth-order high-temperature series expansion (orange) fits for a Heisenberg $S = 1/2$ square lattice model and a $S = 1/2$ frustrated square lattice model with interplanar coupling J_3, respectively, to (b) χ_m and (c) zero-field specific heat C_p, simultaneously. The resulting model parameters are $J_1 = 6.42(1)$ for the QMC $S = 1/2$ square lattice model and $J_1 = 6.80(1)$ K, $J_2/J_1 = 0.11$, $J_3 = 0$, and $\chi_0 = 1.19 \times 10^{-4}$ for the HTE $S = 1/2$ FSL model.

B. Magnetic Susceptibility and Specific Heat

The temperature dependencies of the molar magnetic susceptibility, χ_m, the inverse molar susceptibility, χ_m^{-1}, and the zero-field specific heat, C_p, of α are shown in Fig. 3. At 280 K, a broad feature is observed in the derivatives of both χ_m and C_p [Fig. S2]. Given its small amplitude and the porosity of the square network of α, we ascribe this feature to the freezing of the lattice water position. A similar feature has been observed in the specific heat data of $(CH_3NH_3)_2NaTi_3F_{12}$[56] and has been attributed to the ordering of the methylammonium groups. Above 50 K, χ_m is well described by a modified Curie-Weiss (CW) law, $\chi_m(T) = C/(T - \theta_{CW}) + \chi_0$, where $C = N_A\mu_{eff}^2/3k_B$ and θ_{CW} are the Curie and Weiss constants, respectively, and χ_0 is a temperature independent background term. Relatively weak antiferromagnetic interactions are suggested as χ_m is consistently best described by $\theta_{CW} = -7.86(1)$ K. We also find a positive $\chi_0 = 1.19(2) \times 10^{-4}$ emu mol^{-1}, as seen in other Ti^{3+}-containing compounds[57, 58] which may be ascribed to a van Vleck contribution to the susceptibility[59]. The fitted Curie constant, $C = 0.233(1)$ emu K mol^{-1}, reveals a reduced effective magnetic moment, $\mu_{eff} = 1.36(1)\ \mu_B$ ($g = 1.57(1)$), in comparison to the $S = 1/2$ spin-only moment, $\mu_{eff} = 1.73\ \mu_B$. As discussed in Sec. V, although a reduction of the effective moment in Ti^{3+}-containing compounds is usually a consequence of an orbital contribution, this picture is probably not applicable for α. Instead, considering the instability of Ti^{3+} in air, it may reflect the presence of a minor impurity phase, for example an oxidized surface layer of the polycrystalline sample, or a data normalization problem arising from the non-stoichiometry of α. Indeed, this is not uncommon for Ti^{3+}-containing compounds, where a similar reduction in g, unassociated with an orbital contribution[60, 61], is observed for both $KTi(SO_4)_2$ [62] and $KTi(SO_4)_2{\cdot}H_2O$ [63]. Finally, it should be noted that the possible pres-

TABLE I. Single crystal XRD data and structural refinement parameters for α-$KTi(C_2O_4)_2{\cdot}xH_2O$ and β-$KTi(C_2O_4)_2{\cdot}2H_2O$.

Compound	α-$KTi(C_2O_4)_2{\cdot}xH_2O$	β-$KTi(C_2O_4)_2{\cdot}2H_2O$
Formula weight/g mol^{-1}	299.03	299.03
Temperature / K	150	150
Crystal system	Tetragonal	Hexagonal
Space group	$I4/mcm$	$P6_222$ (or $P6_422$)
a / Å	8.0401(4)	8.7926(4)
b / Å	8.0401(4)	8.7926(4)
c / Å	14.8504(13)	11.1247(5)
α / °	90	90
β / °	90	90
γ / °	90	120
V / Å^3	959.98(13)	744.82(8)
Z	8	3
Crystal size / mm^3	0.07 × 0.07 × 0.03	0.12 × 0.06 × 0.05
Color	Orange	Maroon
ρ / g cm^{-3}	2.069	2.000
F(000)	596.0	447.0
Reflections collected	3279	5932
Independent reflections	287 [R_{int} = 0.0614, R_σ = 0.0252]	512 [R_{int} = 0.0432, R_σ = 0.0186]
Goodness-of-fit on F^2	1.091	1.087
Final R indexes [I>=2σ(I)]	R_1 = 0.0453, wR_2 = 0.1112	R_1 = 0.0214, wR_2 = 0.0509

TABLE II. Refined $I4/mcm$ structural model of α-$KTi(C_2O_4)_2{\cdot}1.48(4)D_2O$ as obtained from the analysis of HRPD data (χ^2 = 4.80, R_p = 2.83%) at 1.8 K. The unit cell parameters are $a = b = 8.043(1)$ Å and $c = 14.719(1)$ Å.

Atom	Site	x	y	z	$Occ.$	U_{iso} (Å^2)
Ti	4a	0.0000	0.0000	0.2500	1.0	0.0066(8)
K	8h	0.3753(5)	0.1247(5)	0.5000	0.5	0.0137(10)
O1	32m	0.2098(1)	0.0931(1)	0.3277(6)	1.0	0.0065(2)
O2	16k	0.2836(3)	0.9232(3)	0.5000	0.37(1)	0.0065(2)
C1	16l	0.2836(1)	0.2164(1)	0.2954(8)	1.0	0.0060(2)
D	32m	0.2531(1)	0.9907(3)	0.5514(2)	0.37(1)	0.0363(1)

ence of a magnetic ion deficiency was examined by allowing a free occupancy refinement of the Ti^{3+} and K^+ sites in the models considered using both the PND and SC-XRD data. While it cannot be conclusively disregarded, it is highly unlikely that a deficiency exists as the resulting goodness-of-fit parameters worsen (χ^2 = 7.13 and R_p = 3.23%), and only models with instead an insignificant Ti^{3+} excess of 1.4(1.3)% were extracted.

Upon cooling, the build up of short-range antiferromagnetic correlations is evidenced by a broad maximum in χ_m centered around 6.1 K. This signature is also observed in the specific heat at a slightly lower temperature, as is typical for low-dimensional square lattice systems[8]. No features indicative of long-range magnetic order can be observed in either data-set down to 1.8 K. Because of the non-stoichiometric nature of α, the values of the molar susceptibility and specific heat should be treated as approximate, and have been calculated with respect to the hydration of the deuterated sample obtained from the HRPD refinement.

To estimate the magnitude of the leading magnetic exchange parameter in α, J_1, a QMC simulation was performed for the Heisenberg $S = 1/2$ square lattice model using the `ALPS`[49, 50] simulation package. By approximating the phonon contribution to the specific heat using $C_p = \alpha T^3 + \beta T^5 + \gamma T^7$, as done with other coordination frameworks[64, 65], a simultaneous fit to χ_m and C_p above 5 K yields J_1 = 6.42(1) K (g = 1.53(1)) when χ_0 is fixed to its CW fit value. Given that the QMC method is not generally applicable to frustrated systems, the `HTE10` code[51] was used to calculate the [4,6] Padé approximant of the high-temperature-series expansion of a $S = 1/2$ FSL model, with two in-plane exchange interactions, J_1 and J_2, and an interplanar coupling, J_3 [Fig. 2(c)]. Using a similar simultaneous fitting procedure above 7 K, the magnetic susceptibility and specific heat data were best described by a slightly frustrated system ($J_2/J_1 = 0.11$) with J_1 = 6.80(1) K (g = 1.61) and no interplanar coupling. The fitting parameters were J_1 and the coefficients of the phonon contribution, while J_2 and J_3 were varied in $0.01J_1$ steps between $-0.2J_1$ and $0.3J_1$, and χ_0 was fixed to its CW fit value. The absence of significant interplanar coupling, $J_3/J_1 < 1.9 \times 10^{-3}$, is further implied by applying the empirical formula $T_N = (4\pi\rho_s)/(b - \ln(J_3/J_1))$[66] for $T_N < 1.8$ K (see Sec. IV C). Finally, as discussed in the methodology of the DFT calculations (Sec. II) where a similar magnetic behavior is observed regardless of the model used to describe structural disorder, the extent of hydration and disorder in the potassium and water containing layers separating the $[Ti(C_2O_4)_2]^-$ planes indeed appear to be inconsequential to the magnetism of the ti-

tanium oxalate containing layers, as similar CW, QMC, and HTE parameters were extracted when fitting χ_m of another α sample [Fig. S2].

At first glance, the solution extracted from the HTE fit is more consistent with the expected $\theta_{CW} = (J_1 + J_2)/k_B = 7.55(2)$ K for a FSL system than the QMC fit. This is further corroborated when considering the residual plots of both fits, as the HTE model better describes the experimental data over the whole fitting range [Fig. S4]. Our DFT calculations furthermore estimate that Ti-Ti exchanges beyond the nearest-neighbor are at least an order of magnitude smaller than J_1. As such, distinguishing between the two solutions provided by HTE and QMC will require probes such as inelastic neutron scattering, which are beyond the scope of this current study. Regardless, the dominant antiferromagnetic nearest-neighbor interactions and possible slight frustration indicate that α belongs to the Néel ordered region of the FSL phase diagram [4].

C. Magnetic Structure

To investigate the nature of the low-temperature magnetic state of α, PND data were collected at regular temperature intervals between 1.2 K and 15 K on the WISH instrument at ISIS. No magnetic features were present in the subtracted data above 2 K, placing 1.2 K $< T_N <$ 1.8 K. Given the small ordered moment expected for a quasi-two-dimensional quantum spin system, the analysis was performed on the magnetic-only scattering obtained by subtracting the 15 K data set from that collected at 1.2 K. Two magnetic Bragg peaks were observed at positions corresponding to forbidden nuclear positions of the $I4/mcm$ space group [Fig. 1(b)] and were thus indexed by the commensurate propagation vector $\mathbf{k} = (0, 0, 0)$. To determine the magnetic structure, four irreducible representations—$m\Gamma_{3+}$, $m\Gamma_{3-}$, $m\Gamma_{5+}$, and $m\Gamma_{5-}$ in Miller-Love notation [67]—were found to be compatible with the paramagnetic space group and propagation vector using the `BasIreps`[46] and `MAXMAGN`[68] software packages. Of these, $m\Gamma_{3+}$ and $m\Gamma_{5+}$ correspond to ferromagnetic structures, and are therefore incompatible with the magnetic susceptibility of α. Indeed, by refining the nuclear structural model to data collected at 15 K ($R_p = 5.24\%$, $Occ._{\mathrm{D_2O}} = 0.40(2)$) and fixing the resulting structural and instrumental parameters for the magnetic model refinement, only the magnetic space group $I4/m'cm$ (in Belov-Neronova-Smirnova notation [69]) belonging to $m\Gamma_{3-}$, correctly describes the data ($\chi^2 = 1.82, R_{mag} = 3.16\%$) [Fig. 1(b)]. Comparative Rietveld plots for the other possible models are presented in Fig. S5.

The resulting magnetic structure is shown in Fig. 2(c) and can be described as a G-type antiferromagnet with the magnetic moments aligned along the c axis. The two-dimensional character of α-$KTi(C_2O_4)_2{\cdot}xD_2O$ is corroborated by the observed ordered moment $\mu = 0.62(3)$ μ_B per Ti^{3+} extracted from the Rietveld fit, similar to other square network systems[5, 70, 71], and to the expected ordered moment of 0.6 μ_B for a $S = 1/2$ square lattice antiferromagnet [72–74]. The discrepancy between the value extracted from the fit to PND data and the expected $gS\mu_B = 0.81$ μ_B extracted from the HTE fit is most likely associated with data renormalization issues as discussed in Sec. IV B. Also, given that the exact Néel temperature is unknown, thermal effects, resulting in the reduction of the ordered moment, cannot be excluded as the origin of the moment reduction.

IV. RESULTS FOR β-$KTi(C_2O_4)_2{\cdot}2H_2O$

A. Crystal Structure

A chiral hexagonal $P6_222$ crystal structure of β was determined through the analysis of SC-XRD data collected at 150 K, as summarised in Table. I. This is consistent with the reported structure of the related β-$NH_4Ti(C_2O_4)_2{\cdot}2H_2O$, whereby the chirality of the crystal structure is such that both enantiomers, $P6_222$[34] and $P6_422$[75], are reported depending on the particular single crystal studied. A multi-bank refinement of this model to PND data collected on HRPD further confirms this structure at all measured temperatures [Fig. 4(a)] and gives an overall $\chi^2 = 3.06$ and $R_p = 1.81\%$ at 1.8 K with the model shown in Table. III. Because of the chirality of the crystal structure of β, standard powder diffraction measurements cannot distinguish between the enantiomers as polycrystalline samples are most likely comprised of a racemic mixture of the enantiomorphic space group pair[76]. As illustrated in Fig. 5(a), the crystal structure of β forms a three-dimensional diamond-like network of Ti^{3+} ions in a distorted square antiprismatic configuration linked by oxalate groups [Fig. 5(b)]. The distortion arises from the presence of two oxalate oxygen sites, giving rise to four Ti-O1 and two Ti-O2 bonds with distances of 2.11(3) Å and 2.27(2) Å, respectively. Each oxalate group coordinates two Ti^{3+} ions, thus providing a pathway for nearest-neighbour superexchange, J_1, with a Ti-Ti distance of 5.75(2) Å. Next-nearest-neighbour exchanges J_2, J_3, and J_4 run along the $\langle 111 \rangle$, $\langle 100 \rangle$, and $\langle 010 \rangle$ directions with similar Ti-Ti distances of 8.46(2) Å, 8.63(1) Å, and 8.78(3) Å, respectively [Fig. 5(c)]. Along the c axis, K^+ ions and water molecules are packed in a column-like manner within the cavities surrounding the diamond-like sublattice [Fig. S6]. Water molecules are present on the O3 site and form hydrogen bonds with the O2 site of the oxalate groups at a distance of 1.92(2) Å.

B. Magnetic Susceptibility and Specific Heat

The temperature-dependent molar magnetic susceptibility, χ_m, effective magnetic moment, μ_{eff}, and specific heat, C_p, of β are shown in Fig. 6. Fitting χ_m over the

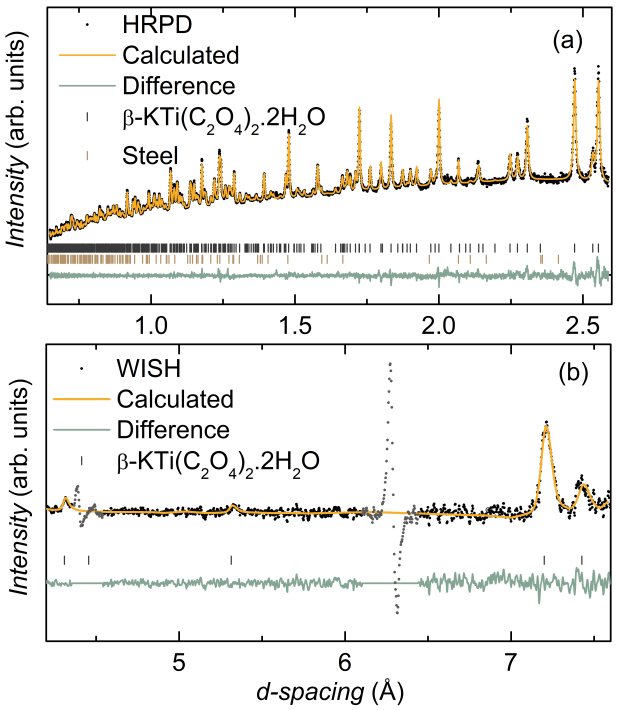

FIG. 4. (a) Rietveld plot for data collected on HRPD at 1.8 K using the $P6_222$ structural model to describe β-$KTi(C_2O_4)_2{\cdot}2H_2O$ with goodness-of-fit parameters R_p = 1.81% and χ^2 = 3.06. (b) Rietveld refinement (R_{mag} = 1.93%, χ^2 = 3.91) of the P_b2_1 magnetic space group model to magnetic-only scattering obtained by subtracting data collected on the WISH instrument at 35 K and 1.2 K. In both plots, data points are shown in black, fitted curves in orange, difference curves in blue, Bragg reflection positions in grey and brown, and excluded data points in grey.

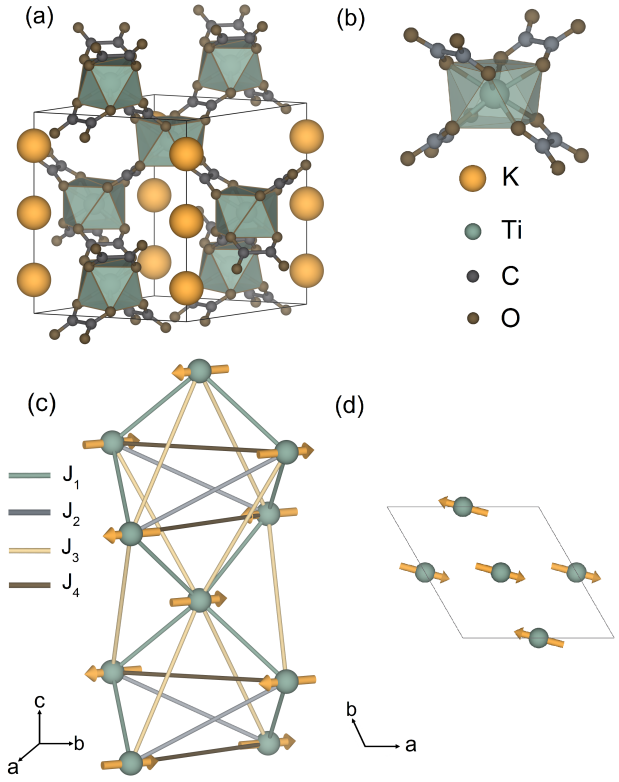

FIG. 5. (a) The crystal structure of β-$KTi(C_2O_4)_2{\cdot}2H_2O$ as viewed along the $\langle 111 \rangle$ directions where (b) distorted square antiprismatic Ti^{3+} ions form a diamond-like magnetic sublattice. (c) One of the possible magnetic moment arrangements for the P_b2_1 magnetic structure describing the coplanar antiferromagnetic ordering of β-$KTi(C_2O_4)_2{\cdot}2H_2O$ with the nearest-neighbor and further neighbor exchange interactions shown in blue, gray, yellow, and brown, respectively. The possible spin arrangements only differ with respect to how the moment aligns within the ab plane. The illustrated structure in (d) is representative of one of the possible moment directions.

temperature range 230 K to 300 K with the same modified CW model as applied to α yields $\theta_{CW} = -109.6(1)$ K and $C = 0.329(1)$ emu K mol^{-1} (g = 1.87). The resulting negative θ_{CW} indicates dominant antiferromagnetic interactions an order of magnitude larger than those of α. A reduced $\mu_{eff} = 1.62(1)\ \mu_B$ is calculated from C, which is consistent with a previous report [77], and its deviation from the spin-only moment—combined with the observed temperature dependence of the magnetic moment and relatively large negative θ_{CW}—likely reflects the presence of antiferromagnetic correlations above 200 K. We also find a small and negative $\chi_0 = -4.88(3) \times 10^{-5}$ emu mol^{-1}, indicating the contribution of the sample holder and core diamagnetism of β to the total magnetic susceptibility. The presence of short-range correlations is evidenced by a broad maximum in χ_m centered about 43 K, followed by an inflection point at 28 K that can be attributed to long-range antiferromagnetic ordering. This ordering transition is also present as an anomaly in C_p at the same temperature [Fig. 6(c)].

To estimate the nearest-neighbor exchange interaction

TABLE III. Crystallographic data for β-$KTi(C_2O_4)_2{\cdot}2H_2O$ as obtained by fitting the $P6_222$ model to data collected on HRPD at 1.8 K. The unit cell parameters are $a = b$ = 8.784(1) Å and c = 11.148(2) Å and the goodness-of-fit parameters are χ^2 = 3.06 and R_p = 1.81%.

Atom	Site	x	y	z	U_{iso} (Å^2)
Ti	3d	0.5000	0.0000	0.5000	0.0012(6)
K	3b	0.0000	0.0000	0.5000	0.0019(2)
O1	12k	0.2656(2)	0.9210(2)	0.4001(1)	0.0068(2)
O2	12k	0.4494(2)	0.7615(2)	0.3923(1)	0.0063(2)
O3	6g	0.7662(3)	0.7662(3)	0.3333	0.0093(5)
C1	6i	0.2094(1)	0.7906(1)	0.3333	0.0055(5)
C2	6i	0.3083(1)	0.6917(1)	0.3333	0.0050(5)
H	12k	0.7493(5)	0.6574(4)	0.3152(3)	0.0330(8)

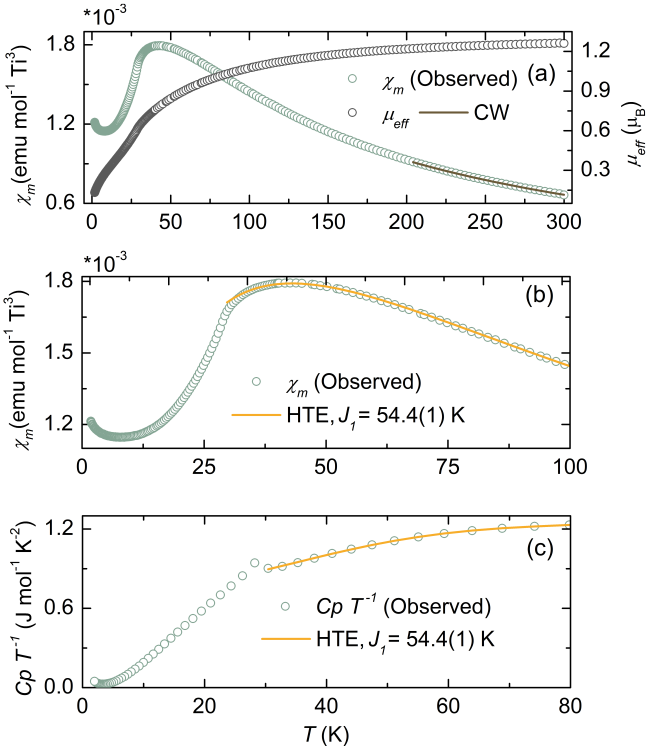

FIG. 6. (a) Zero-field cooled magnetic susceptibility of β-$KTi(C_2O_4)_2{\cdot}2H_2O$, χ_m (blue), of measured between 1.8 K and 300 K in a 0.1 T applied magnetic field and corresponding calculated effective magnetic moment (grey). A Curie-Weiss fit to χ_m (brown) yields $\theta_{CW} = -109.6(1)$ K, $C = 0.329(2)$ emu K mol^{-1}, and $\chi_0 = -4.88(3)\times10^{-5}$ emu mol^{-1}. (b) and (c) Simultaneous fit to χ_m and the zero-field specific heat C_pT^{-1} using the diamond lattice model with a nearest-neighbor coupling J_1 calculated by a tenth-order high-temperature series expansion. The model yields $J = 54.4(1)$ K and $\chi_0 = -4.11(8)\times10^{-5}$ emu mol^{-1}.

in β, J_1, the diamond lattice model was used to simultaneously fit χ_m and C_p using the same HTE fitting procedure applied for α. Above 60 K, the data were consistently best described by a leading exchange $J_1 = 54.4(1)$ K ($g = 1.74$) and a temperature independent background term $\chi_0 = -4.11(8)\times10^{-5}$ emu mol^{-1}, similar to that extracted from the CW fit. Interestingly, the resulting $T_N/J_1 = 0.51$ ratio is similar to the theoretically predicted ratio, $T_N/J_1 = 0.531(1)$[78], expected for a $S = 1/2$ Heisenberg diamond lattice model system. A frustrated diamond lattice model extended to account for further near-neighbor couplings was also used to simultaneously fit χ_m and C_p [Fig. S5]. While the resulting parameters ($J_2/J_1 = 0.04$, $J_3/J_1 = 0.03$, $J_4/J_1 = 0.04$, and $g = 1.78$) better describe χ_m [Fig. S7], this model should be taken at best as suggestive of frustration given the number of exchange parameters involved. Together with T_N, the fitted parameters are broadly consistent with minimal frustration and place β within the Néel ordered region of the FDL phase diagram [79].

C. Magnetic Structure

Indeed, the onset of three-dimensional magnetic order in β is verified by the presence of additional intensity in the subtracted PND data (1.2 K − 35 K) [Fig. 4(b)]. The observed magnetic reflections can be indexed by a unit cell doubled along the c axis with the propagation vector $\mathbf{k} = (0, 0, 1/2)$. Symmetry analysis using `ISODISTORT`[80] and `SARAh`[81] reveal five irreducible representations, mA$_1$, mA$_3$, mA$_4$, mA$_5$, and mA$_6$, compatible with $\mathbf{k}$ and the nuclear space group, $P6_222$ (or $P6_422$). However, all magnetic models given by these irreducible representations, except for mA$_6$, conflict with the presence of $(00l)$-type reflections in the PND data.

Accordingly, the best description of the data ($R_{mag} = 1.93\%$, $\chi^2 = 3.91$), shown in Fig. 4(b), is obtained with using the P_b2_1 magnetic space group of the mA$_6$ irreducible representation. The resulting ordered moment, $\mu = 0.79(2)$ μ_B, is similar to the theoretically expected value, $\mu = 0.76$ μ_B[78], for the $S = 1/2$ Heisenberg diamond lattice model, and is slightly suppressed from the expected $gS\mu_B = 0.87$ μ_B from the susceptibility fits. Interestingly, and in contrast to previous studies on $S = 1/2$ diamond lattice systems[82, 83], β is the first system in which the ordered moment of the $S = 1/2$ diamond lattice model can be extracted without any ambiguity related to possible orbital contributions and/or covalency effects. The reasons for this are further discussed in Sec. V. Comparative fits with other possible models are presented in Fig. S8. It should be noted that the magnetic moment direction of the P_b2_1 structure in the ab plane cannot be uniquely determined from the present data alone, because the structure factor of the strongest (101) peak at $d \sim 7.2$ Å is insensitive to the in-plane moment direction. A representative illustration of the magnetic structure, in which nearest-neighbor (J) magnetic moments are antiferromagnetic and align along the ab plane, is therefore shown in Figs. 5 (c) and (d). The full determination of the magnetic ground state of β would be challenging even with a deuterated single crystal due to the 12 domains created by the lowering of symmetry from $P6_2221'$ (or $P6_4221'$) to P_b2_1. Given that the structure of β is chiral, it should also be noted that the analysis of polycrystalline PND data is insensitive to the enantiomorphic space group pair, and an enantiopure single crystal would be necessary for further analysis.

V. DISCUSSION

One of the most striking observations made in comparing the magnetic properties of α and β is the substantial difference between the magnitudes of their nearest-neighbor exchange interactions. Indeed, the nearest-neighbor exchange parameter, J_1, in the diamond network of Ti^{3+} ions in β is an order of magnitude larger than the corresponding leading exchange for α. To understand the

origin of this behavior, one has to consider the nature of the orbitals involved in the respective superexchange pathways of α and β and how they overlap. For a transition metal ion in the square antiprismatic coordination environment exhibited in α and β, the crystal field symmetry splits the degenerate d-orbitals into a low-lying A_1 (d_{z^2}) ground state term and two higher energy levels corresponding to the doubly degenerate E_2 and E_3 terms[84]. In the case of a Ti^{3+} ion in such an environment, the lone $3d^1$ electron is thus expected to populate the d_{z^2} orbital within the A_1 ground state. Indeed, through our DFT band-structure calculations, we identify d_{z^2} as the active magnetic orbital for both α and β, even in the presence of the distorted square antiprismatic coordination environment found in the latter, as also observed for β-$NH_4Ti(C_2O_4)_2{\cdot}2H_2O$[75].

As described in the context of several other oxalate-based coordination frameworks, the interplay between the architecture of the oxalate-metal bridge and the active magnetic orbital plays a crucial role in determining the sign and strength of the resulting exchange[85, 86]. In the case of α, these oxalate bridges lie within the plane of the Ti^{3+} ions, whereas the oxalate bridging in β spans different planes. As illustrated through the calculated Wannier functions in Fig. 7, this leads to a significant superexchange in β, where the d_{z^2} orbital overlaps directly with the oxalate π-bonding orbital. This results in a contribution to the exchange pathway at the C atoms within the oxalate bridge where the magnetic orbitals of the neighboring Ti^{3+} ions overlap. Conversely, when the active orbital is parallel to the oxalate group—as is more often discussed in the context of a $d_{x^2-y^2}$ active orbital in Cu^{2+}-containing compounds—a significantly reduced exchange interaction is expected[85, 86]. This appears to be the case for α, in which the Ti^{3+} d_{z^2} orbital overlaps with a different molecular orbital with minimal contribution at the C atoms, resulting in a reduced overlap with the neighboring Ti^{3+} ion, and thus a weaker superexchange interaction.

While the effect of spin-orbit coupling is expected to be pronounced for octahedrally coordinated Ti^{3+}-containing compounds[87], our DFT results also reveal a negligible contribution from orbitally excited states for the square antipristmatic coordination of Ti^{3+} in α and β. This is unsurprising given the d_{z^2} ($m_l = 0$) ground state. The combination of this result and our experimental observations indicate that α and β should be considered close to ideal model $S = 1/2$ Heisenberg square and diamond lattice antiferromagnets, respectively.

Compared with other coordination frameworks, the magnetic response of α resembles that seen in the square lattice antiferromagnet, $Cu(pz)_2(ClO_4)_2$ (pz = pyrazine), where $J_2/J_1 \approx 0.02$[33, 88]. Given the relatively large distances between the magnetic ion centers in such systems, the weak frustration present in both α and $Cu(pz)_2(ClO_4)_2$ is to be expected. As a consequence, while some advantages are associated with coordination frameworks, especially related to tuning the energy scales present in the system through different bridging molecules, designing frustration into them is more difficult in comparison to their oxide counterparts. This is a result of the complex exchange pathways, which require several sets of orbitals to align favorably to generate an appreciable exchange. As for β, to the best of our knowledge, this is the first comprehensive study of the magnetic properties of a diamond lattice coordination framework, especially one in which the magnetic ion resides in an 8-coordinate environment. However, the extracted nearest-neighbour exchange parameter, J_1, is of the same order of magnitude as that of $Ti_2(C_2O_4)_3(H_2O)_5$ ($J = 86$ K)[89], and the magnetic response of β bears resemblance to that of the A-site diamond lattice spinel, $CoRh_2O_4$[22].

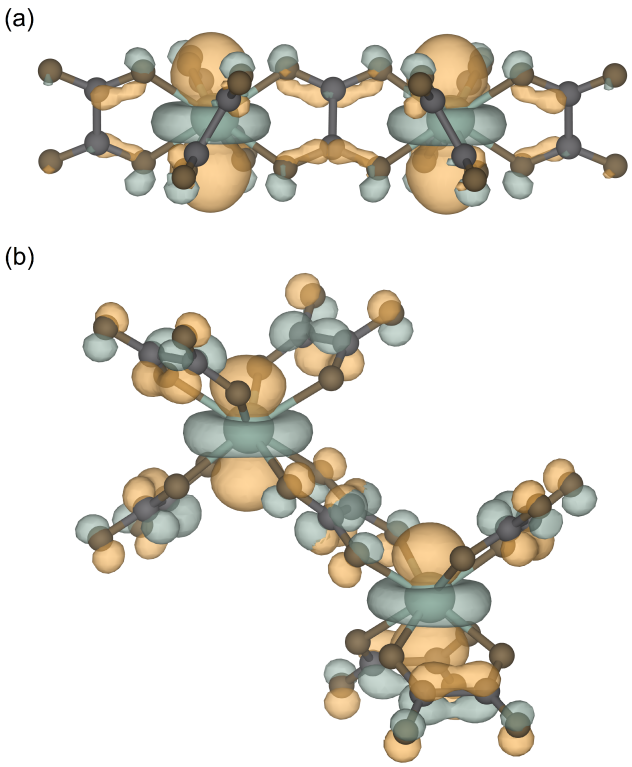

FIG. 7. Ti^{3+} d_{z^2}-based Wannier functions showing the orbital overlaps for the J_1 superexchange pathways of (a) α-$KTi(C_2O_4)_2{\cdot}xH_2O$ and (b) β-$KTi(C_2O_4)_2{\cdot}2H_2O$.

VI. CONCLUSIONS

In summary, we have presented a detailed investigation of the crystallographic and magnetic properties of the Ti^{3+}-containing coordination frameworks, α-$KTi(C_2O_4)_2{\cdot}xH_2O$ and β-$KTi(C_2O_4)_2{\cdot}2H_2O$. Through analysis of SC-XRD and PND data, a quasi-two-dimensional square planar network of Ti^{3+} ions was found within the crystal structure of α. β, on the other hand, realises a three-dimensional diamond-like array of

Ti^{3+} moments. Bulk characterization indicates slight frustration of the antiferromagnetic interactions present in both systems, and simultaneous fits to the magnetic susceptibility and specific heat data demonstrate the two-dimensional character of the magnetic correlations in α. Concomitantly, the order of magnitude difference in the extracted exchange parameters manifests the stark differences in the orbital interactions at play in each of the psuedo-polymorphs. Through supporting DFT calculations, these differences can be understood as arising from the different bridging geometries between neighboring Ti^{3+} ions, which result in different orbital overlaps between the d_{z^2}-orbitals and the oxalate π bonding orbitals. At low temperatures, the onset of long-range antiferromagnetic order was verified for both systems in PND data, with the resulting magnetic structures and ordered moments identifying α and β as realizations of $S = 1/2$ Heisenberg square and diamond lattice antiferromagnetic models, respectively.

Given the rarity of stable Ti^{3+}-based compounds and the versatility of coordination frameworks, we hope our results provide a pathway towards future experiments to further understand the observed magnetic behavior. Inelastic neutron scattering, for example, will provide a more detailed picture of the exchange Hamiltonian in both systems, and also access to exotic quantum phenomena like magnetic field-induced spontaneous decay of magnons in the square lattice antiferromagnet [90, 91]. For this purpose, the development of new synthetic routes for the growth of large single crystals will be necessary. Further understanding of the complex crystal structure of α may also be gleaned from single crystal neutron diffraction measurements combined with thermogravimetric analysis. As several crystallographic studies on $AM(C_2O_4)\cdot 2H_2O$ ($A = NH_4$[34, 75, 77], Na[35], Rb[35], K[36, 77, 92], Cs[37], and M = Ti, In[93]) already exist, it may prove fruitful to explore how the various energy scales involved in this family of materials can be tuned by varying the monovalent ion site. Finally, the roles of spin and orbital contributions to the magnetic properties of these models could be explored by varying the transition metal ions contained within the coordination framework from Ti^{3+} ($S = 1/2$) to V^{3+} ($S = 1$), Mo^{3+} ($S = 3/2$), or Fe^{3+} ($S = 5/2$).

VII. ACKNOWLEDGEMENTS

Provision of a PhD studentship to A.H.A. by the University of Liverpool and the Science and Technology Facilities Council (STFC) is gratefully acknowledged. The work of T.L. was funded by the University of St Andrews and China Scholarship Council (CSC) joint scholarship (201606280032). A.T. was funded by the Federal Ministry of Education and Research through the Sofja Kovalevskaya Award of Alexander von Humboldt Foundation. Work at St Andrews was supported by the Leverhulme Trust (RPG-2013-343). The authors are also grateful to the STFC for access to neutron beamtime at ISIS and thank Dr. Gavin Stenning for aiding with SQUID and specific heat measurements at the Materials Characterization Laboratory, ISIS. We thank Dr. Manh Duc Le (ISIS), Dr. Ross Stewart (ISIS), Dr. Craig Robertson (Uni. Liverpool), Dr. Samantha Chong (Uni. Liverpool), and Dr. Hamish Yeung (Uni. Birmingham) for useful discussions.

[1] A. Harrison, First catch your hare: the design and synthesis of frustrated magnets, J. Phys. Condens. Matter **16**, S553 (2004).

[2] A. Vasiliev, O. Volkova, E. Zvereva, and M. Markina, Milestones of low-D quantum magnetism, npj Quantum Mater. **3**, 18 (2018).

[3] J. G. Rau, E. K.-H. Lee, and H.-Y. Kee, Spin-orbit physics giving rise to novel phases in correlated systems: iridates and related materials, Annu. Rev. Condens. Matter Phys **7**, 195 (2016).

[4] N. Shannon, B. Schmidt, K. Penc, and P. Thalmeier, Finite temperature properties and frustrated ferromagnetism in a square lattice Heisenberg model, Eur. Phys. J. B **38**, 599 (2004).

[5] A. Bombardi, J. Rodriguez-Carvajal, S. Di Matteo, F. de Bergevin, L. Paolasini, P. Carretta, P. Millet, and R. Caciuffo, Direct determination of the magnetic ground state in the square lattice $S = 1/2$ antiferromagnet Li_2VOSiO_4, Phys. Rev. Lett. **93**, 27202 (2004).

[6] R. Nath, A. A. Tsirlin, H. Rosner, and C. Geibel, Magnetic properties of $BaCdVO(PO_4)_2$: A strongly frustrated spin-1/2 square lattice close to the quantum critical regime, Phys. Rev. B **78**, 64422 (2008).

[7] A. A. Tsirlin, A. A. Belik, R. V. Shpanchenko, E. V. Antipov, E. Takayama-Muromachi, and H. Rosner, Frustrated spin-1/2 square lattice in the layered perovskite $PbVO_3$, Phys. Rev. B **77**, 92402 (2008).

[8] A. A. Tsirlin, R. Nath, A. M. Abakumov, Y. Furukawa, D. C. Johnston, M. Hemmida, H.-A. Krug von Nidda, A. Loidl, C. Geibel, and H. Rosner, Phase separation and frustrated square lattice magnetism of $Na_{1.5}VOPO_4F_{0.5}$, Phys. Rev. B **84**, 14429 (2011).

[9] A. Tsirlin, O. Janson, S. Lebernegg, and H. Rosner, Square-lattice magnetism of diaboleite $Pb_2Cu(OH)_4Cl_2$, Phys. Rev. B **87** (2013).

[10] L. Yang, M. Jeong, P. Babkevich, V. M. Katukuri, B. Náfrádi, N. E. Shaik, A. Magrez, H. Berger, J. Schefer, E. Ressouche, M. Kriener, I. Živković, O. V. Yazyev, L. Forró, and H. M. Rønnow, J_1-J_2 square lattice antiferromagnetism in the orbitally quenched insulator $MoOPO_4$, Phys. Rev. B **96**, 24445 (2017).

[11] H. Ishikawa, N. Nakamura, M. Yoshida, M. Takigawa, P. Babkevich, N. Qureshi, H. M. Rønnow, T. Yajima, and Z. Hiroi, J_1-J_2 square-lattice Heisenberg antiferromagnets with $4d^1$ spins: AMoOPO$_4$Cl (A=K,Rb), Phys. Rev. B **95**, 64408 (2017).

[12] O. Mustonen, S. Vasala, K. P. Schmidt, E. Sadrollahi, H. C. Walker, I. Terasaki, F. J. Litterst, E. Baggio-Saitovitch, and M. Karppinen, Tuning the $S = 1/2$ square-lattice antiferromagnet $Sr_2Cu(Te_{(1-x)}W_x)O_6$ from Néel order to quantum disorder to columnar order, Phys. Rev. B **98**, 64411 (2018).

[13] O. Mustonen, S. Vasala, H. Mutch, C. I. Thomas, G. B. G. Stenning, E. Baggio-Saitovitch, E. J. Cussen, and M. Karppinen, Magnetic interactions in the $S = 1/2$ square-lattice antiferromagnets Ba_2CuTeO_6 and Ba_2CuWO_6: parent phases of a possible spin liquid, ChemComm **55**, 1132 (2019).

[14] P. Chandra and B. Doucot, Possible spin-liquid state at large S for the frustrated square Heisenberg lattice, Phys. Rev. B **38**, 9335 (1988).

[15] F. Mezzacapo, Ground-state phase diagram of the quantum J_1-J_2 model on the square lattice, Phys. Rev. B **86**, 45115 (2012).

[16] D. Poilblanc, M. Mambrini, and S. Capponi, Critical colored-RVB states in the frustrated quantum Heisenberg model on the square lattice, SciPost Phys. **7**, 41 (2019).

[17] O. Mustonen, S. Vasala, E. Sadrollahi, K. P. Schmidt, C. Baines, H. C. Walker, I. Terasaki, F. J. Litterst, E. Baggio-Saitovitch, and M. Karppinen, Spin-liquid-like state in a spin-1/2 square-lattice antiferromagnet perovskite induced by d^{10}–d^0 cation mixing, Nat. Commun. **9**, 1085 (2018).

[18] M. Skoulatos, F. Rucker, G. J. Nilsen, A. Bertin, E. Pomjakushina, J. Ollivier, A. Schneidewind, R. Georgii, O. Zaharko, L. Keller, C. Rüegg, C. Pfleiderer, B. Schmidt, N. Shannon, A. Kriele, A. Senyshyn, and A. Smerald, Putative spin-nematic phase in $BaCdVO(PO_4)_2$, Phys. Rev. B **100**, 14405 (2019).

[19] K. Y. Povarov, V. K. Bhartiya, Z. Yan, and A. Zheludev, Thermodynamics of a frustrated quantum magnet on a square lattice, Phys. Rev. B **99**, 24413 (2019).

[20] A. Smerald, Magnon binding in $BaCdVO(PO_4)_2$, arXiv:2003.12747 [cond-mat.str-el] (2020).

[21] B. Danu, G. Nambiar, and R. Ganesh, Extended degeneracy and order by disorder in the square lattice J_1-J_2-J_3 model, Phys. Rev. B **94**, 94438 (2016).

[22] L. Ge, J. Flynn, J. A. M. Paddison, M. B. Stone, S. Calder, M. A. Subramanian, A. P. Ramirez, and M. Mourigal, Spin order and dynamics in the diamond-lattice Heisenberg antiferromagnets $CuRh_2O_4$ and $CoRh_2O_4$, Phys. Rev. B **96**, 64413 (2017).

[23] G. J. MacDougall, D. Gout, J. L. Zarestky, G. Ehlers, A. Podlesnyak, M. A. McGuire, D. Mandrus, and S. E. Nagler, Kinetically inhibited order in a diamond-lattice antiferromagnet, Proc. Natl. Acad. Sci. U.S.A. **108**, 15693 LP (2011).

[24] S. Gao, O. Zaharko, V. Tsurkan, Y. Su, J. S. White, G. Tucker, B. Roessli, F. Bourdarot, R. Sibille, D. Chernyshov, T. Fennell, A. Loidl, and C. Rüegg, Spiral spin-liquid and the emergence of a vortex-like state in $MnSc_2S_4$, Nat. Phys. **13**, 157 (2017).

[25] D. Bergman, J. Alicea, E. Gull, S. Trebst, and L. Balents, Order-by-disorder and spiral spin-liquid in frustrated diamond-lattice antiferromagnets, Nat. Phys. **3**, 487 (2007).

[26] N. Tristan, J. Hemberger, A. Krimmel, H.-A. Krug von Nidda, V. Tsurkan, and A. Loidl, Geometric frustration in the cubic spinels MAl_2O_4 (M=Co, Fe, and Mn), Phys. Rev. B **72**, 174404 (2005).

[27] G. Chen, L. Balents, and A. P. Schnyder, Spin-orbital singlet and quantum critical point on the diamond lattice: $FeSc_2S_4$, Phys. Rev. Lett. **102**, 96406 (2009).

[28] G. Chen, A. P. Schnyder, and L. Balents, Excitation spectrum and magnetic field effects in a quantum critical spin-orbital system: The case of $FeSc_2S_4$, Phys. Rev. B **80**, 224409 (2009).

[29] V. Tsurkan, L. Prodan, V. Felea, I. Filippova, V. Kravtsov, A. Günther, S. Widmann, H.-A. Krug von Nidda, J. Deisenhofer, and A. Loidl, Structure, magnetic susceptibility, and specific heat of the spin-orbital-liquid candidate $FeSc_2S_4$: influence of Fe off-stoichiometry, Phys. Rev. B **96**, 54417 (2017).

[30] K. Tustain, L. Farrar, W. Yao, P. Lightfoot, I. da Silva, M. T. F. Telling, and L. Clark, Materialization of a geometrically frustrated magnet in a hybrid coordination framework: a study of the iron(II) oxalate fluoride framework, $KFe(C_2O_4)F$, Inorg. Chem. **58**, 11971 (2019).

[31] C. N. R. Rao, A. K. Cheetham, and A. Thirumurugan, Hybrid inorganic-organic materials: a new family in condensed matter physics, J. Phys.: Condens. Matter **20**, 159801 (2008).

[32] Y.-Z. Zheng, M.-L. Tong, W. Xue, W.-X. Zhang, X.-M. Chen, F. Grandjean, and G. Long, A "star" antiferromagnet: a polymeric iron(III) acetate that exhibits both spin frustration and long-range magnetic ordering, Angew. Chem. Int. Ed. **46**, 6076 (2007).

[33] N. Tsyrulin, F. Xiao, A. Schneidewind, P. Link, H. M. Rønnow, J. Gavilano, C. P. Landee, M. M. Turnbull, and M. Kenzelmann, Two-dimensional square-lattice $S = 1/2$ antiferromagnet $Cu(pz)_2(ClO_4)_2$, Phys. Rev. B **81** (2010).

[34] R. B. English and D. J. Eve, Ammonium di-μ-oxalatotitanate(III) dihydrate: an eight-coordinate, polymeric titanium(III) complex, Inorg. Chim. Acta **203**, 219 (1993).

[35] M. G. B. Drew and D. J. Eve, Observations on the spectra and structures of seven-and eight-co-ordinate oxalato complexes of titanium(III), Inorg. Chim. Acta **25**, L111 (1977).

[36] A. Stähler, Zur Kenntniss des Titans. II. (Zum Theil gemeinsam mit Heinz Wirthwein), Ber. Dtsch. Chem. Ges. **38**, 2619 (1905).

[37] M. G. B. Drew and D. J. Eve, Caesium triaquabis(oxalato)titanate(III) dihydrate, Acta Crystallogr. B **33**, 2919 (1977).

[38] G. Sheldrick, SHELXT - Integrated space-group and crystal-structure determination, Acta Crystallogr. A **71**, 3 (2015).

[39] G. Sheldrick, Crystal structure refinement with SHELXL, Acta Crystallogr. C **71**, 3 (2015).

[40] L. Clark, P. Lightfoot, A. Gibbs, G. Nilsen, and L. Farrar, Structural, orbital and magnetic orders in the alpha- and beta-phases of $S = 1/2$ $KTi(C_2O_4)_2{\cdot}2H_2O$ - a neutron diffraction study, STFC ISIS Neutron and Muon Source (2018).

[41] R. M. Ibberson, Design and performance of the new supermirror guide on HRPD at ISIS, Nucl. Instrum. Methods Phys. Res **600**, 47 (2009).

[42] L. Clark, A. Abdeldaim, K. Tustain, and J. Graham, Magnetic orders in the alpha- and beta-Phases of $S = 1/2$ $KTi(C_2O_4)_2{\cdot}2H_2O$, STFC ISIS Neutron and Muon Source (2020).

[43] L. C. Chapon, P. Manuel, P. G. Radaelli, C. Benson, L. Perrott, S. Ansell, N. J. Rhodes, D. Raspino, D. Duxbury, E. Spill, and J. Norris, Wish: the new powder and single crystal magnetic diffractometer on the second target station, Neutron News **22**, 22 (2011).

[44] B. H. Toby, Expgui, a graphical user interface for gsas, J. Appl. Crystallogr **34**, 210 (2001).

[45] A. C. Larson and R. B. von Dreele, Los Alamos National Laboratory Report LAUR 86-748 (2004).

[46] J. Rodríguez-Carvajal, Recent advances in magnetic structure determination by neutron powder diffraction, Physica B **192**, 55 (1993).

[47] S. Todo and K. Kato, Cluster Algorithms for General-S Quantum Spin Systems, Phys. Rev. Lett. **87**, 47203 (2001).

[48] H. G. Evertz, The loop algorithm, Adv. Phys. **52**, 1 (2003).

[49] B. Bauer, L. D. Carr, H. G. Evertz, A. Feiguin, J. Freire, S. Fuchs, L. Gamper, J. Gukelberger, E. Gull, S. Guertler, A. Hehn, R. Igarashi, S. V. Isakov, D. Koop, P. N. Ma, P. Mates, H. Matsuo, O. Parcollet, G. Pawłowski, J. D. Picon, L. Pollet, E. Santos, V. W. Scarola, U. Schollwöck, C. Silva, B. Surer, S. Todo, S. Trebst, M. Troyer, M. L. Wall, P. Werner, and S. Wessel, The ALPS project release 2.0: open source software for strongly correlated systems, J. Stat. Mech. Theory Exp. **2011**, P05001 (2011).

[50] A. Albuquerque, F. Alet, P. Corboz, P. Dayal, A. Feiguin, S. Fuchs, L. Gamper, E. Gull, S. Gürtler, A. Honecker, R. Igarashi, M. Körner, A. Kozhevnikov, A. Läuchli, S. Manmana, M. Matsumoto, I. McCulloch, F. Michel, R. Noack, G. Pawłowski, L. Pollet, T. Pruschke, U. Schollwöck, S. Todo, S. Trebst, M. Troyer, P. Werner, and S. Wessel, The ALPS project release 1.3: open-source software for strongly correlated systems, J. Magn. Magn. Mater **310**, 1187 (2007).

[51] A. Lohmann, H.-J. Schmidt, and J. Richter, Tenth-order high-temperature expansion for the susceptibility and the specific heat of spin-s Heisenberg models with arbitrary exchange patterns: application to pyrochlore and kagome magnets, Phys. Rev. B **89**, 014415 (2014).

[52] K. Koepernik and H. Eschrig, Full-potential nonorthogonal local-orbital minimum-basis band-structure scheme, Phys. Rev. B **59**, 1743 (1999).

[53] J. P. Perdew and Y. Wang, Accurate and simple analytic representation of the electron-gas correlation energy, Phys. Rev. B **45**, 13244 (1992).

[54] See Supplemental Material at http://link.aps.org/supplemental/ 10.1103/PhysRevMaterials.xx.xxxxxx for further details on DFT calculations and outputs, modeling of magnetic susceptibility and heat capacity data, and fitting results of all symmetry allowed magnetic models to powder neutron diffraction data.

[55] K. Momma and F. Izumi, *VESTA 3* for three-dimensional visualization of crystal, volumetric and morphology data, J. Appl. Cryst. **44**, 1272 (2011).

[56] N. Jiang, A. Ramanathan, J. Bacsa, and H. S. La Pierre, Synthesis of a d^1-titanium fluoride kagome lattice antiferromagnet, Nat. Chem. **12**, 691 (2020).

[57] R. L. Aggarwal, A. Sanchez, R. E. Fahey, and A. J. Strauss, Magnetic and optical measurements on Ti:Al_2O_3 crystals for laser applications: Concentration and absorption cross section of Ti^{3+} ions, Appl. Phys. Lett. **48**, 1345 (1986).

[58] M. Eitel and J. Greedan, A high resolution neutron diffraction study of the perovskite $LaTiO_3$, J. Less-Common Met. **116**, 95 (1986).

[59] P. H. Carr and S. Foner, Magnetic Transitions in Ti_2O_3 and V_2O_3, Int. J. Appl. Phys. **31**, S344 (1960).

[60] D. Kasinathan, K. Koepernik, O. Janson, G. J. Nilsen, J. O. Piatek, H. M. Rønnow, and H. Rosner, Electronic structure of $KTi(SO_4)_2{\cdot}H_2O$: an $S = 1/2$ frustrated chain antiferromagnet, Phys. Rev. B **88** (2013).

[61] G. J. Nilsen, A. Raja, A. A. Tsirlin, H. Mutka, D. Kasinathan, C. Ritter, and H. M. Rønnow, One-dimensional quantum magnetism in the anhydrous alum $KTi(SO_4)_2$, New J. Phys **17**, 113035 (2015).

[62] S. T. Bramwell, S. G. Carling, C. J. Harding, K. D. M. Harris, B. M. Kariuki, L. Nixon, and I. P. Parkin, The anhydrous alums as model triangular-lattice magnets, J. Phys.: Condens. Matter **8**, L123 (1996).

[63] G. J. Nilsen, H. M. Rønnow, A. M. Läuchli, F. P. A. Fabbiani, J. Sanchez-Benitez, K. V. Kamenev, and A. Harrison, A new realisation of the $S = 1/2$ frustrated chain antiferromagnet, Chem. Mater **20**, 8 (2008).

[64] T. Lancaster, S. J. Blundell, M. L. Brooks, P. J. Baker, F. L. Pratt, J. L. Manson, M. M. Conner, F. Xiao, C. P. Landee, F. A. Chaves, S. Soriano, M. A. Novak, T. P. Papageorgiou, A. D. Bianchi, T. Herrmannsdörfer, J. Wosnitza, and J. A. Schlueter, Magnetic order in the $S = 1/2$ two-dimensional molecular antiferromagnet copper pyrazine perchlorate $Cu(Pz)_2(ClO_4)_2$, Phys. Rev. B **75**, 94421 (2007).

[65] R. Nath, M. Padmanabhan, S. Baby, A. Thirumurugan, D. Ehlers, M. Hemmida, H.-A. Krug von Nidda, and A. A. Tsirlin, Quasi-two-dimensional $Cu[C_6H_2(COO)_4][C_2H_5NH_3]_2$, Phys. Rev. B **91**, 54409 (2015).

[66] C. Yasuda, S. Todo, K. Hukushima, F. Alet, M. Keller, M. Troyer, and H. Takayama, Néel temperature of quasi-low-dimensional Heisenberg antiferromagnets, Phys. Rev. Lett. **94**, 217201 (2005).

[67] S. C. Miller and W. F. Love, *Tables of irreducible representations of space groups and co-representations of magnetic space groups* (Boulder, Colo: Pruett Press, 1967).

[68] J. Perez-Mato, S. Gallego, E. Tasci, L. Elcoro, G. de la Flor, and M. Aroyo, Symmetry-based computational tools for magnetic crystallography, Annu. Rev. Mater. Res. **45**, 217 (2015).

[69] N. Belov, N. Neronova, and T. Smirnova, Shubnikov groups, Kristallografiya **2**, 315 (1957).

[70] S. Bettler, F. Landolt, Ö. M. Aksoy, Z. Yan, S. Gvasaliya, Y. Qiu, E. Ressouche, K. Beauvois, S. Raymond, A. N. Ponomaryov, S. A. Zvyagin, and A. Zheludev, Magnetic structure and spin waves in the frustrated ferro-antiferromagnet $Pb_2VO(PO_4)_2$, Phys. Rev. B , 184437.

[71] T. Koga, N. Kurita, M. Avdeev, S. Danilkin, T. J. Sato, and H. Tanaka, Magnetic structure of the $S = 1/2$ quasi-two-dimensional square-lattice Heisenberg antiferromagnet Sr_2CuTeO_6, Phys. Rev. B **93**, 054426 (2016).

[72] E. Manousakis, The spin-1/2 Heisenberg antiferromagnet on a square lattice and its application to the cuprous oxides, Rev. Mod. Phys. **63**, 1 (1991).

[73] B.-G. Liu, Low-temperature properties of the quasi-two-dimensional antiferromagnetic Heisenberg model, Phys. Rev. B **41**, 9563 (1990).

[74] M. Holt, O. Sushkov, D. Stanek, and G. Uhrig, Three-dimensional generalization of the J_1-J_2 Heisenberg model on a square lattice and role of the interlayer coupling J_c, Phys. Rev. B **83** (2011).

[75] H. S. Sheu, J. C. Wu, Y. Wang, and R. B. English, Charge density studies in $NH_4[Ti(C_2O_4)_2].2H_2O$ crystals at two wavelengths, Acta Crystallogr. B **52**, 458 (1996).

[76] S. Fujio, K. Tanaka, and H. Inui, Formation probability for enantiomorphic crystals (with the space groups of $P6_222$ and $P6_422$) in transition-metal disilicides with the C40 structure as determined by convergent-beam electron diffraction, Intermetallics **15**, 245 (2007).

[77] V. T. Kalinnikov, V. V. Zelentsov, A. A. Zharkikh, and T. G. Aminov, The magnetic susceptibilities of complex Ti(III) oxalates, Bull. Acad. Sci. USSR, Div. Chem. Sci. **18**, 2670 (1969).

[78] J. Oitmaa, Diamond lattice Heisenberg antiferromagnet, J. Phys. Condens. Matter **30**, 155801 (2018).

[79] J. Oitmaa, Frustrated diamond lattice antiferromagnet, Phys. Rev. B **99**, 134407 (2019).

[80] B. J. Campbell, H. T. Stokes, D. E. Tanner, and D. M. Hatch, ISODISPLACE: a web-based tool for exploring structural distortions, J. Appl. Crystallogr **39**, 607 (2006).

[81] A. S. Wills, A new protocol for the determination of magnetic structures using simulated annealing and representational analysis (SARAh), Physica B Condens. Matter **276-278**, 680 (2000).

[82] C. A. Marjerrison, C. Mauws, A. Z. Sharma, C. R. Wiebe, S. Derakhshan, C. Boyer, B. D. Gaulin, and J. E. Greedan, Structure and Magnetic Properties of $KRuO_4$, Inorg. Chem. **55**, 12897 (2016).

[83] S. Injac, A. K. L. Yuen, M. Avdeev, F. Orlandi, and B. J. Kennedy, Structural and magnetic studies of $KOsO_4$, a $5d^1$ quantum magnet oxide, Phys. Chem. Chem. Phys. **21**, 7261 (2019).

[84] M. Randić, Ligand field splitting of d-orbitals in eight coordinated complexes of square antiprism structure, Croat. Chem. Acta **32**, 189 (1960).

[85] O. Kahn, Dinuclear complexes with predictable magnetic properties, Angew. Chem. **24**, 834 (1985).

[86] J. Cano, P. Alemany, S. Alvarez, M. Verdaguer, and E. Ruiz, Exchange coupling in oxalato-bridged copper(II) binuclear compounds: a density functional study, Chem. Eur. J **4**, 476 (1998).

[87] R. L. Carlin, *Magnetochemistry* (Springer-Verlag Berlin Heidelberg, 1986).

[88] N. Tsyrulin, T. Pardini, R. R. P. Singh, F. Xiao, P. Link, A. Schneidewind, A. Hiess, C. P. Landee, M. M. Turnbull, and M. Kenzelmann, Quantum effects in a weakly frustrated $S = 1/2$ two-dimensional Heisenberg antiferromagnet in an applied magnetic field, Phys. Rev. Lett. **102**, 197201 (2009).

[89] J. T. Wrobleski and D. B. Brown, A study of the variable-temperature magnetic susceptibility of two Ti(III) oxalate complexes, Inorg. Chim. Acta **38**, 227 (1980).

[90] M. E. Zhitomirsky and A. L. Chernyshev, Instability of antiferromagnetic magnons in strong fields, Phys. Rev. Lett. **82**, 4536 (1999).

[91] O. F. Syljuåsen, Numerical evidence for unstable magnons at high fields in the Heisenberg antiferromagnet on the square lattice, Phys. Rev. B **78**, 180413 (2008).

[92] D. J. Eve and G. W. A. Fowles, Oxalate complexes of tervalent titanium, J. Chem. Soc , 1183 (1966).

[93] N. Bulc, L. Golic, and J. Siftar, Structure of ammonium and sodium bis(oxalato)indate(III) dihydrate, $NH_4[In(C_2O_4)_2]\cdot 2H_2O$ and $Na[In(C_2O_4)_2]\cdot 2H_2O$, Acta Crystallogr. C **39**, 176 (1983).